Measurement Quality Metrics for Rapid Laser Range

MacKinnon, David; Blais, François; Aitken, Victor

Publisher's version / la version de l'éditeur:
SPIE Journal of Electronic Imaging, 19, Number 1, 2010-08-01

Measurement Quality Metrics for Rapid Laser Range Scanning

David MacKinnon* and François Blais†

Institute for Information Technology, National Research Council of Canada

Victor Aitken‡

Department of Systems and Computer Engineering, Carleton University

(Dated: June 18, 2009)

Quality metrics quantify by how much some aspect of a measurement deviates from a predefined standard. Measurement quality evaluations of laser range scanner data are used to perform range image registration, merging measurements, and view planning. We have developed a scanning method that uses laser range scanner quality metrics to both reduce the time required to obtain a complete range image from a single viewpoint and the number of measurements obtained during the scanning process. This approach requires a laser range scanner capable of varying both the area and sampling density of individual scans, but can be combined with view planning methods to reduce the total time required to obtain a complete surface map of an object. Several new quality metrics are introduced: outlier, resolvability, planarity, integration, return, and enclosed quality metrics. These metrics are used as part of a quality-based merge method, referred to here as a quality-weighted modified Kalman minimum variance (weighted-MKMV) estimation method. Experimental evidence is presented confirming that this approach can significantly reduce the total scanning time. This approach may be particularly useful for rapidly generating CAD models of real-world objects.

I. INTRODUCTION

Measurement quality evaluations are becoming increasingly important in laser range imaging for a variety of applications; however, a recent survey [1] of laser range scanner quality metrics identified several unresolved issues with regard to quantifying laser range scanner quality mea-

*Electronic address: David.MacKinnon@nrc-cnrc.gc.ca

†Electronic address: Francois.Blais@nrc-cnrc.gc.ca

‡Electronic address: Victor.Aitken@sce.carleton.ca

surements. According to the survey, no quality metric exists to address the affect on laser range scanner measurement quality of beam footprint motion during acquisition, measurement resolution, or the presence of non-return measurements. A series of new quality metrics are presented in this paper to address these issues, as well as some that were not identified in [1]: surface planarity and the effect of data processing on measurement quality.

Measurement quality metrics have rarely been used to drive the measurement acquisition process. Sequeira et al. [2] used quality metrics to more effectively merge overlapping range images and as part of the view planning process. Callieri et al. [3] used quality metrics for view planning as part of a multi-stage approach. This approach, first developed by Scott et al. [4] for small-volume scanning, involved acquiring an initial low-density scan which was then used to plan a series of viewpoints from which to acquire high-density scans.

A multi-stage method is presented in this paper in which quality metrics are used to minimize the time required to acquire a range image from a single viewpoint while maximizing the overall quality of the final range image. This is accomplished by scanning only the areas of the total field of view in which it is likely that a high-density scan would improve the final range image obtained from that viewpoint. Experiments using this method demonstrate that both the time required to acquire a high-quality range image and the total number of measurements acquired can be significantly reduced when compared to that required to acquire a single high-density range image. Figure 1 shows the setup used to perform all experiments. Reducing the number of measurements can reduce post-processing time and, by extension, reduce the time between initial acquisition and final model generation. This scanning method is well-suited for either fully-automated scanning systems or systems that guide a minimally-trained operator.

II. RANGE MEASUREMENT QUALITY METRICS

The quality of a laser range scanner measurement depends on measurement uncertainty and measurement resolution; however, spatial uncertainty is also strongly affected by other environmental factors such as the type of surface material [5], surface reflectivity [6], distance to the surface [6, 7], and incidence angle [8]. The purpose of a quality metric is to quantify some aspect of the quality of a laser range scanner measurement with respect to some previously-established benchmark. No attempt has been made to establish optimal benchmark values for the quality metrics used in this paper because benchmark values are application and scanner specific so must be

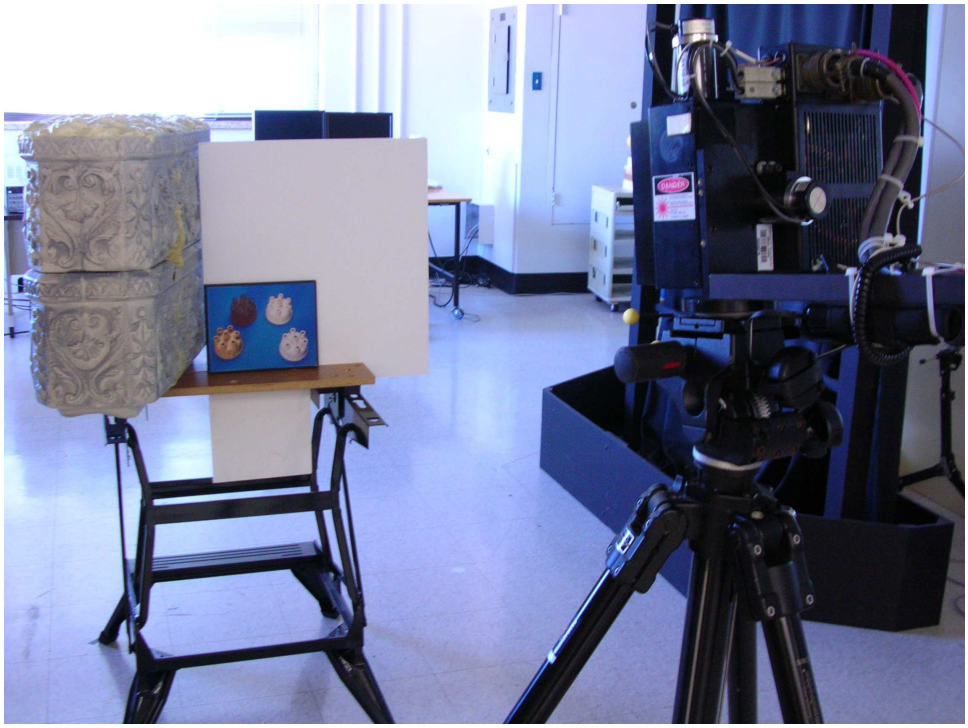

Figure 1: Experimental setup

established on a case-by-case basis. The benchmark values used in this paper have been obtained for the laser range scanner used in this experiment for the purpose of minimizing model acquisition time.

In this section, we introduce a series of quality metrics $c_i^{metric} \in [0,1]$ for laser range scanner measurements. All quality metrics presented in this paper use the range $c_i^{metric} = 1$ (ideal quality) to $c_i^{metric} = 0$ (unacceptable quality) where the term "metric" refers to any quality metric presented in this paper. In some cases, the quality metric associated with a measurement $\mathbf{p}_i$ is defined relative to its neighbourhood in the range image. The neighbourhood $N(\mathbf{p}_i)$ of a range image measurement $\mathbf{p}_i$ is broadly defined as a set of K_i measurements $\{\mathbf{p}_j, \ldots, \mathbf{p}_{j+K_i-1}\}$ that are neighbours of $\mathbf{p}_i$ according to some previously-defined neighbourhood criteria. The neighbourhood criteria used to define $N(\mathbf{p}_i)$ depends on how the range image is constructed; for example, $N(\mathbf{p}_i)$ for a range image consisting of a regular grid of measurements can be defined as all range image measurements immediately adjacent to $\mathbf{p}_i$. In this case, measurements on the interior of this range image would have exactly $K_i = 8$ neighbours while those on the boundary would have either $K_i = 3$ or $K_i = 6$ neighbours.

A. Return Quality Metric

The return quality metric c_i^{return} indicates whether the measurement has a valid range and intensity value. A measurement should ideally have a valid range and intensity value so would be assigned $c_i^{return} = 1$; otherwise, it would be assigned $c_i^{return} = 0$. Measurements in which $c_i^{return} = 1$ are defined as Return measurements because the laser range scanner measurement arises from a return signal that could be converted by the scanning system into a range and intensity value. Measurements in which $c_i^{return} = 0$ are defined as Non-return measurement and can be the result of either insufficient return signal intensity or a return signal that saturates the detector. In the case of time-of-flight systems, it can also mean that no return signal was detected during the ambiguity interval [7]. All other quality metrics describing $\mathbf{p}_i$ are assigned $c_i^{metric} = 0$ if $c_i^{return} = 0$.

B. Enclosed Quality Metric

In some situations, reported values arise from neighbourhood-based procedures. For example, some of the metrics presented here, as well as many data processing procedures, use all the neighbours of a measurement. If some of those neighbours are Non-return measurements, or if the measurement is on the boundary of a range image, then the reported values may be based on an insufficient or asymmetric data set. A measurement is defined as an Enclosed measurement if all neighbours of the measurement are Return measurements and the measurement is not on the boundary of the range image. If a measurement is an Enclosed measurement then it is assigned $c_i^{enc} = 1$; otherwise, it is assigned $c_i^{enc} = 0$ and is defined as a Non-enclosed measurement [9, 10].

C. Outlier Quality Metric

The outlier quality metric c_i^{out} represents the effect of data processing on the quality of range and intensity measurements. Data processing involves activities like smoothing that are intended to improve the range image by reducing the effect of measurement noise; however, data processing can, and often does, change the measurement value v_i associated with $\mathbf{p}_i$. In some cases, this change can be significantly greater than what would be expected based on experimentally-determined measurement uncertainty s_V. If $\Delta v_i = |v_i^{raw} - v_i^{processed}|$, where v_i^{raw} is the original (raw data) measurement and $v_i^{processed}$ is the processed measurement, is greater than the two-tailed error margin v_i^{err} [11, pp.696] then $\mathbf{p}_i$ has less than ideal quality [9, 10].

The quality metric c_i^{out} is the minimum, or worst-case, of the range outlier quality metric $c_{i,R}^{out}$ and the intensity outlier quality metric $c_{i,I}^{out}$. The quality metric c_i^{out} is found using

$$c_i^{out} = \min\{c_{i,R}^{out}, c_{i,I}^{out}\} \tag{1}$$

where

$$c_{i,R}^{out} = \begin{cases} 1 & \Delta R_i \leq R_i^{err} \\ \dfrac{R_i^{err}}{\Delta R_i} & \text{otherwise} \end{cases} \tag{2}$$

and

$$c_{i,I}^{out} = \begin{cases} 1 & \Delta I_i \leq I_i^{err} \\ \dfrac{I_i^{err}}{\Delta I_i} & \text{otherwise} \end{cases} \tag{3}$$

are the range ($v = R$) and intensity ($v = I$) outlier quality metrics respectively [9, 10]. A simple ratio model was employed to make it easy for a minimally-trained operator to interpret the graphical representation of c_i^{out}. This metric is dependent upon the type of data processing that is used so when stating the outlier quality it must be made clear what data processing procedures separate the raw and processed results. Data processing procedures like averaging and median filtering are neighbourhood-based procedures so the quality of c_i^{out} can be assessed using c_i^{enc}.

D. Planarity Quality Metric

The planarity quality metric c_i^{plane} indicates whether the surface within $N(\mathbf{p}_i)$ is locally-planar, based on whether $\mathbf{p}_i$ is contained within a locally-planar neighbourhood [12]. Measurements arising from planar surfaces are considered to be of ideal quality because there are no discontinuities to introduce measurement error, so are assigned $c_i^{plane} = 1$, ; otherwise, they are assigned $c_i^{plane} = 0$. Measurements in which $c_i^{plane} = 1$ are defined as Planar measurements, meaning that the measurement arises from a planar surface, and measurements in which $c_i^{plane} = 0$ are defined as Non-planar measurements [9, 10]. The metric c_i^{plane} is a neighbourhood-based metric so its quality can be assessed using c_i^{enc}.

E. Resolvability Quality Metric

The resolvability quality metric c_i^{res} is used to identify regions that cannot be resolved at the target surface resolution Δx to within a margin of error given the current scanner viewpoint. The

beam should ideally intersect a surface close enough to the scanner, and with a sufficiently low surface orientation, that the width of the beam footprint is less than Δx. If it is likely that the width of the beam footprint is too large to resolve surface details to at least Δx then any measurement arising from this surface is considered to be of unacceptable quality. The quality metric c_i^{res} is found by

$$c_i^{res} = \begin{cases} 1 & d_i^{length} \leq d_i^{up} \\ \dfrac{d_i^{up} - d_i^{width}}{d_i^{length} - d_i^{width}} & d_i^{width} < d_i^{up} < d_i^{length} \\ 0 & d_i^{up} \leq d_i^{width} \end{cases} \tag{4}$$

where d_i^{width} is the width of the short axis of the beam footprint, d_i^{length} is the length of the long axis of the beam footprint, and $d_i^{up} = \Delta x + 2d_i^{err}$ is the target surface resolution with an error margin based on the measurement rotational uncertainty [9, 10]. All three terms are illustrated in Figure 2. The length of the long axis of the beam footprint is found by $d_i^{length} = d_i^{max} + d_i^{min}$, the sum of components of the long axis. For a Gaussian beam, these components are found using

$$\{d_i^{min}, d_i^{max}\} = \left| \frac{-K_{i,2} \pm \sqrt{K_{i,2}^2 - 4K_{i,1}K_{i,3}}}{2K_{i,1}} \right| \tag{5}$$

where

$$\begin{aligned} K_{i,1} &= [w(0)\sin(\rho_i)]^2 - [\zeta_0 \cos(\rho_i)]^2 \\ K_{i,2} &= 2\zeta_i w^2(0)\sin(\rho_i) \\ K_{i,3} &= [w(0)\zeta_0]^2 + [w(0)\zeta_i]^2 \end{aligned} \tag{6}$$

and are illustrated in Figure 2 [9, 10]. The $w(0)$ term represents the predicted radius of the beam waist, ζ_i is the radial distance from the beam waist, ρ_i is the angle between the surface normal estimate $\vec{n}_i$ and the laser path $\vec{r}_i$, and ζ_0 is the depth of focus [13]. The derivation of (5) can be found in Appendix A and applies only to Gaussian beam being transmitted through a medium with negligible effect on beam spread [14, 15]. The error term d_i^{err} is added to the surface distance from the beam footprint centre to the beam footprint edge to ensure that the scanner is close enough to the surface to resolve features to at least Δx with a margin of error. To simplify the equation, the surface is assumed to be locally-planar so the quality of c_i^{res} can be assessed using c_i^{plane}. This error term is found using

$$d_i^{err} = \frac{R\sin(\theta_{err})}{\cos(\gamma_i) - \sin(\gamma_i)\sin(\theta_{err})} \tag{7}$$

in which the rotational error term θ_{err} is defined as

$$\theta_{err} = \sqrt{\chi^2(1,\alpha)(\max\{s_\theta^2, s_\phi^2\})} \tag{8}$$

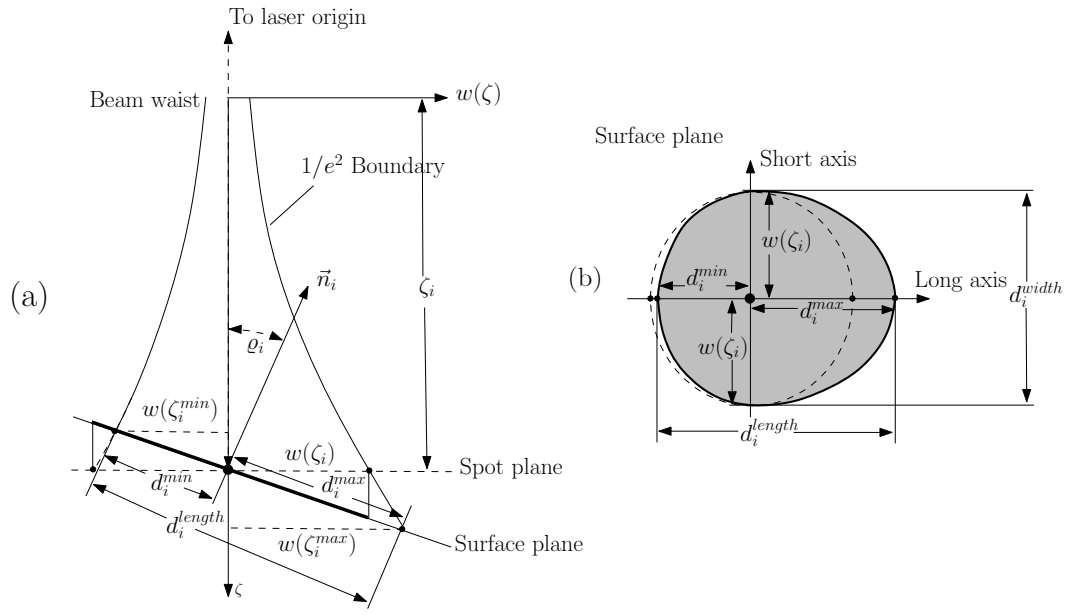

Figure 2: Beam intersection with an angled planar surface results in an oval beam footprint with length d_i^{length} and width $2w(\zeta_i)$ where ζ_i is the distance from the surface to the beam waist along the beam axis. (a) Side view with short axis directed outward from the page (b) top view with normal directed outward from the page.

where $\chi^2(1,\alpha)$ is the chi-squared statistic with significance level α and one degree of freedom, and s_θ and s_ϕ are the experimentally-determined horizontal (θ) and vertical (ϕ) rotational uncertainties. The θ_{err} term represents the maximum rotational distance between two points, in this case the centre of one beam footprint and the edge of its neighbouring beam footprint, such that they can still be considered likely to represent the same point to within a confidence level determined by α given the expected rotational uncertainty of the scanner [9, 10].

All measurements with $c_i^{res} = 0$ are defined as Unresolvable measurements, meaning that surface features cannot be resolved at Δx for these measurements, those with $1 > c_i^{res} > 0$ are defined as Resolvable measurements, and measurements with $c_i^{res} = 1$ are defined as Completely-resolvable measurements [9, 10]. The range (c_i^{range}) and orientation (c_i^{orient}) quality metrics, discussed in Section II G, complement c_i^{res} when defining the bounds of the scannable region. The quality metric c_i^{plane} is a neighbourhood-based metric because it is based on an estimate of the surface normal so its quality can be assessed using c_i^{enc}.

F. Blur Quality Metric

The blur quality metric c_i^{blur} represents the blurring of a laser range scanner measurement as a result of the motion of the beam footprint during acquisition. Measurement uncertainty in triangulation laser range scanners is typically reduced by integrating a single measurement over several intensity samples to counter the effect of speckle noise [16, 17] as illustrated in Figure 3. Blurring can also occur in continuous-wave scanners because the beam footprint is moving during acquisition of the reflected beam peak, but pulse time-of-flight scanners use short pulse lengths so the likelihood of measurement blurring is minimal unless multi-pulse integration is employed to reduce measurement uncertainty. Ideally, the integration distance should be zero to avoid measurement blurring.

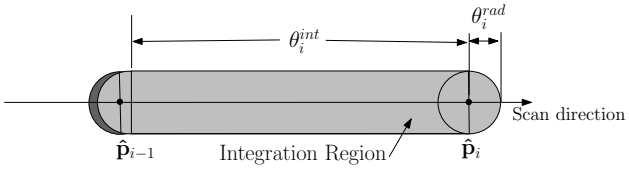

Figure 3: The range measurement uncertainty of laser range scanners is reduced by integrating $\hat{\mathbf{p}}_i$ with instantaneous beam footprint radius θ_i^{rad} over a distance θ_i^{int}. Integration consists of combining multiple samples into a single measurement.

The blur quality metric c_i^{blur} is obtained using

$$c_i^{blur} = \begin{cases} 1 & \theta_i^{int} = 0 \\ \dfrac{\theta_i^{rad}}{\theta_i^{rad} + \theta_i^{int}} & \text{otherwise} \end{cases} \tag{9}$$

where θ_i^{int} is the rotational distance between $\mathbf{p}_i$ and the measurement $\mathbf{p}_{i-1}$ that immediately preceded it in the scan line, and θ_i^{rad} is the radius of the beam footprint in rotational units. The blur metric is assigned $c_i^{blur} = 0$ if $\mathbf{p}_{i-1}$ is not in the same scan line or if $\mathbf{p}_{i-1}$ is a Non-return measurement because there is no way to assess the blur quality without a measurement preceding it in the scan line [9, 10]. A simple ratio model was employed to make it easy for a minimally-trained operator to interpret the graphical representation of c_i^{blur}.

G. Additional Quality Metrics

The orientation quality metric c_i^{orient} is defined as

$$c_i^{orient} = \begin{cases} 0 & \vec{n}_i^T \hat{\mathbf{x}}_i \leq \vec{n}_{max}^T \hat{\mathbf{x}}_i \\ \dfrac{(\vec{n}_i - \vec{n}_{max})^T \hat{\mathbf{x}}_i}{\hat{R}_i - \vec{n}_{max}^T \hat{\mathbf{x}}_i} & \text{otherwise} \end{cases} \tag{10}$$

where $\hat{\mathbf{x}}_i$ is a measurement located a distance $\hat{R}_i$ radially from the viewpoint, $\vec{n}_i$ is the unit normal to the surface at $\hat{\mathbf{x}}_i$, and $\vec{n}_{max}$ is the unit normal for a surface that is oriented ρ_{max}, the user-defined maximum acceptable surface orientation, with respect to the laser path. Measurements with $c_i^{orient} = 0$ are classified as Angled measurements and arise from surfaces that are so highly angled that measurements from them would be discarded during post-processing. Measurements with $c_i^{orient} > 0$ are defined as Non-angled measurements [9, 10]. Surface orientation is a commonly-used quality metric [18–23]; however, previous versions of this metric did not employ a maximum acceptable surface orientation as part of the metric. The metric c_i^{orient} is a neighbourhood-based metric because it is based on an estimate of the surface normal, so its quality can be assessed using c_i^{enc}.

The reflectivity quality metric c_i^{ref} is defined by

$$c_i^{ref} = \begin{cases} 0 & \rho_i \geq \rho_{max} \\ \dfrac{\rho_{max} - \rho_i}{\rho_{max} - 1} & \rho_{max} > \rho_i > 1 \\ 1 & \rho_i = 1 \\ \dfrac{\rho_i - \rho_{min}}{1 - \rho_{min}} & \rho_{min} < \rho_i < 1 \\ 0 & \rho_i \leq \rho_{min} \end{cases} \tag{11}$$

where ρ_{min} and ρ_{max} are user-defined bounds on the acceptable reflectivity of the surface, and ρ_i is the surface reflectivity relative to a reference surface. The surface reflectivity is found using

$$\rho_i = \frac{I_i}{I(R_i)} \tag{12}$$

where I_i is the return signal intensity and $I(R_i)$ is the model-based return signal intensity obtained during calibration. The model-based return signal intensity represents the intensity of the surface used to obtain the models for range and rotational uncertainty [9, 10]. Fiocco et al. [20] had previously defined a reflectivity quality metric as a binary quality metric; however, their approach reduced the generalizability of the metric.

The range quality metric c_i^{range} is defined by

$$c_i^{range} = \begin{cases} 0 & R_i \geq R_{max} \\ \dfrac{R_{max} - R_i}{R_{max} - D(R_i, \theta_i, \phi_i)} & R_{max} > R_i > R_{spot}(\theta_i, \phi_i) \\ 1 & R_i = R_{spot}(\theta_i, \phi_i) \\ \dfrac{R_i - R_{min}}{D(R_i, \theta_i, \phi_i) - R_{min}} & R_{min} < Ri < R_{spot}(\theta_i, \phi_i) \\ 0 & R_i \leq R_{min} \end{cases} \tag{13}$$

where R_{max} is the user-defined maximum acceptable range measurement, R_{min} is the user-defined minimum acceptable range measurement, and $R_{spot}(\theta_i, \phi_i)$ is the distance to the beam waist. The beam diameter orthogonal to the beam axis is smallest at the beam waist so this represents the ideal distance to any surface in the total field of view. Fiocco et al. [20] also defined a distance quality metric based on the minimum and maximum range limits, while Sequeira et al. [2, 18] applied a weighting factor to the range measurement to obtain a quality metric. Measurements with $c_i^{range} = 0$ are defined as Out-of-range measurements.

The sampling quality metric c_i^{sample} represents the likelihood that a scan is sufficiently dense to ensure that features at the desired surface resolution will be detected. The surface distance d_i^{far} from $\mathbf{p}_i$ to the most distant neighbour $\mathbf{p}_j^{max} \in N(\mathbf{p}_i)$ should ideally be within the beam footprint; however, rotational uncertainty makes it impossible to know precisely where the $1/e^2$ boundary intersects the surface. The quality metric c_i^{sample} is defined as a fuzzy transition between most and least probable surface distance to where the $1/e^2$ boundary would intersect the surface. The sampling quality metric is found by

$$c_i^{sample} = \begin{cases} 0 & d_i^{up} \leq d_i^{far} \\ 1 - \dfrac{d_i^{far} - d_i^{low}}{2d_i^{err}} & d_i^{low} < d_i^{far} < d_i^{up} \\ 1 & d_i^{far} \leq d_i^{low} \end{cases} \tag{14}$$

where $\{d_i^{low} = \Delta x - 2d_i^{err}, d_i^{up} = \Delta x + 2d_i^{err}\}$ represent the α-bounds on the target resolution. To simplify the equation, the surface is assumed to be locally-planar so the quality of c_i^{sample} can be assessed using c_i^{plane}. According to the Shannon-Nyquist sampling theorem, the distance between samples must be less than half the smallest feature size to be resolved; otherwise, aliasing distortion occurs [24, pp.142-149]. As a result, measurements with $c_i^{sample} = 0$ are defined as Aliased measurements while those with $c_i^{sample} = 1$ are defined as Non-aliased measurements. All measurements with $1 > c_i^{sample} > 0$ are defined as Partially-aliased measurements [9, 10]. A

simple ratio model was employed to make it easy for a minimally-trained operator to interpret the graphical representation of c_i^{sample}. The metric c_i^{sample} is a neighbourhood-based metric because it assumes a complete neighbourhood in which to find d_i^{far} so its quality can be assessed using c_i^{enc}. Fiocco et al. [20] had previously defined a sampling quality metric based on the distance to the closest neighbour, while Sequeira et al. [2, 18] applied a weighting factor to the average distance the points in a measurement's neighbourhood to obtain a quality metric. Neither approach took into account measurement uncertainty as part of the metric. Moreover, testing the distance to the closest neighbour, or even that average distance, does not ensure that all neighbours are close to the measurement.

H. Total-quality Assessment

A recent survey [1] of laser range scanner quality metrics identified two methods that have been employed for total-quality assessments: weighted-summation and product of binary pass/fails. A composite approach is used in this paper in which all of the quality metrics presented in this section are divided into either exclusive quality metrics or augmenting quality metrics. Exclusive quality metrics are those that must all be acceptable ($c_i^{metric} > 0$) for the total quality of the measurement to be considered acceptable, while augmenting quality metrics are not critical for measurement acceptability but should contribute to the total measurement quality assessment [9, 10]. The total within-scan quality metric c_i^{total} is obtained using

$$c_i^{total} = c_i^{excl}\left(w_{aug}(c_i^{aug} - 1) + 1\right) \tag{15}$$

where $c_i^{aug} \in [0,1]$ is the weighted summation of the augmenting quality metrics, $c_i^{excl} \in [0,1]$ is the product of the exclusive quality metrics, and $w_{aug} \in [0,1]$ is the weighting factor applied to c_i^{aug}.

The exclusive quality metric is the product of those quality metrics that define the bounds of the scannable region. Only measurements with acceptable reflectivity, resolvability, orientation, return, and range quality are within the scannable region so c_i^{excl} takes the form

$$c_i^{excl} = c_i^{ref} c_i^{res} c_i^{orient} c_i^{return} c_i^{range} \ . \tag{16}$$

The remaining metrics are combined to form c_i^{aug}, each of which is weighted based on by how

much they should influence the total quality assessment. The metric c_i^{aug} is found by

$$c_i^{aug} = \frac{w_{plane}c_i^{plane} + w_{enc}c_i^{enc} + w_{blur}c_i^{blur} + w_{sample}c_i^{sample} + w_{out}c_i^{out}}{w_{plane} + w_{enc} + w_{blur} + w_{sample} + w_{out}} \tag{17}$$

where $\left\{w_{plane}, w_{enc}, w_{blur}, w_{sample}, w_{out}\right\} \geq 0$ are the weighting factors applied to each metric. The planarity, enclosed, integration, sampling, and outlier quality of a measurement can be unacceptable and the measurement still remain within the scannable region; however, non-zero quality values indicate a preferred, and therefore higher quality, measurement so they must be included in the total-quality assessment.

III. ADAPTIVE SCANNING

The metrics presented in Section II were used as part of an adaptive scanning method. This method starts with a Delaunay facet map of a low-density anchor scan covering the total field of view. An individual-quality assessment is then performed using the metrics presented in Section II, the results of which are used to divide the facet map into three regions based on the likelihood of obtaining additional useful and non-redundant data about the surface being scanned from that viewpoint. Facets in which all vertices are

- Non-return measurements; or
- Out-of-range measurements

are combined to form the Unscannable region. Facets in which all vertices are Planar measurements are combined to initialize the Complete region, then the remaining facets are used to initialize the Rescan region. Facets in the Complete region are transferred to the Rescan region if:

- they contain reflectivity discontinuities with edge height ΔE_i^{ref} greater than the reflectivity threshold $E_{threshold}^{ref}$;
- at least one vertex is a measurements with $\tilde{c}_i^{out} < c_{threshold}^{out}$ where $c_{threshold}^{out}$ is a threshold value;
- at least one vertex is a Non-return measurement;
- at least one vertex is an Angled measurement; or

- at least one vertex is an Unresolvable measurement

after region initialization. The ΔE_i^{ref} term is the maximum difference in return signal intensity between $\mathbf{p}_i$ and any of its neighbours.

A series of small, high-density subscans is generated to completely cover the Rescan region while minimizing the number of subscans performed. Each subscan is automatically generated with an inter-sample separation θ_{sep} that maximizes the likelihood of achieving Δx while minimizing the number of subscans obtained. The inter-sample separation is defined by

$$\theta_{sep} = \min_{i=1}^{N} \{\theta_i^{\Delta x} - \theta_i^{err}\} \tag{18}$$

where

$$\theta_i^{\Delta x} = \tan^{-1}\left(\frac{\frac{\Delta x}{2}\cos(\gamma_i)}{R_i + \frac{\Delta x}{2}\sin(\gamma_i)}\right) \tag{19}$$

is the rotational distance. The subscans are initially generated using a grid pattern that completely covers the Rescan region, then are moved using an iterative procedure to eliminate redundant scans and minimize coverage of the Unscannable region while ensuring complete Rescan region coverage. A second series of subscans is then performed for facets that

- were not covered by the previous set of subscans; or

- have at least one Non-planar vertex consisting of an Aliased measurement

after the first series of subscans have been merged into the anchor scan to form a composite range image. The merge method is based on the total quality of each measurement and is described in Section III A. The second series of subscans are then merged into the composite range image, a new individual-quality assessment is performed for the points in the composite range image, and a total-quality assessment is performed for the composite range image [9, 10]. The total quality map can then be used to perform view planning, a topic beyond the scope of this paper.

A. Quality-based Measurement Merger

A composite range image (CRI) was initialized with all measurements from the anchor scan. All measurements from each subscan were then extracted and the rotational distance between each subscan measurement and the rotationally closest (corresponding) measurement in the composite range image was determined. Subscan measurements in which the rotational distance was less than

the chi-squared difference between measurements [25, 26] were then selected to be merged using a quality-weighted modified Kalman minimum variance (weighted-MKMV) estimation method.

The weighted-MKMV method involves weighting the covariance matrices with the total within-scan quality associated with the measurement. Given a measurement $\mathbf{p}_{i,CRI}$ in the composite range image with total within-scan quality $c_{i,CRI}^{total}$ and its corresponding subscan measurement $\mathbf{p}_{i,sub}$ with total within-scan quality $c_{i,sub}^{total}$, the measurement $\mathbf{p}_{i,CRI}$ is updated using

$$\begin{aligned} \mathbf{p}_{i,CRI} &= (W_i^{-1} c_{i,CRI}^{total} \Sigma_{i,CRI}^{-1}) \mathbf{p}_{i,CRI} \\ &+ (W_i^{-1} c_{i,sub}^{total} \Sigma_{i,sub}^{-1}) \mathbf{p}_{i,sub} \end{aligned} \tag{20}$$

where

$$W_i = c_{i,CRI}^{total} \Sigma_{i,CRI}^{-1} + c_{i,sub}^{total} \Sigma_{i,sub}^{-1} \tag{21}$$

is the weighting matrix. In these equations, $\Sigma_{i,sub}$ is the covariance of $\mathbf{p}_{i,sub}$ and $\Sigma_{i,CRI}$ is the covariance of measurement $\mathbf{p}_{i,CRI}$, and $c_{i,CRI}^{total}$ and $c_{i,sub}^{total}$ are scalar. The covariance matrix estimate is updated using

$$\Sigma_{i,CRI} = \frac{1}{c_{i,CRI}^{total} + c_{i,sub}^{total}} W_i^{-1} \tag{22}$$

which weights the covariance matrix elements toward the higher-quality measurement [9, 10].

The process of updating the composite range image with each subscan proceeds as follows:

- If $c_{i,CRI}^{total} > 0$ and $c_{i,sub}^{total} > 0$ then the weighted-MKMV method is used.
- If $c_{i,CRI}^{total} = 0$ and $c_{sub,i}^{total} = 0$ then $\mathbf{p}_{i,CRI}$ and $\Sigma_{i,CRI}$ are updated using the MKMV estimator method [23].
- If $c_{i,CRI}^{total} > 0$ and $c_{i,sub}^{total} = 0$ then $\mathbf{p}_{i,CRI}$ and its associated covariance matrix $\Sigma_{i,CRI}$ are unchanged.
- If $c_{i,CRI}^{total} = 0$ and $c_{i,sub}^{total} > 0$ then $\mathbf{p}_{i,CRI}$ is assigned the value of $\mathbf{p}_{i,sub}$ and $\Sigma_{i,CRI}$ is replaced with $\Sigma_{i,sub}$, the covariance matrix associated with $\mathbf{p}_{i,sub}$.

Finally, the total within-scan quality is updated such that

$$c_{i,CRI}^{total} = w_{i,CRI} c_{i,CRI}^{total} + w_{i,sub} c_{i,sub}^{total} \tag{23}$$

where

$$w_{i,CRI} = \frac{c_{i,CRI}^{total}}{w_i \sigma(\mathbf{p}_{i,sub} | \mathbf{p}_{i,CRI}, \Sigma_{i,CRI})^2} \tag{24}$$

and

$$w_{i,subscan} = \frac{c_{i,sub}^{total}}{w_i \sigma(\mathbf{p}_{i,CRI}|\mathbf{p}_{i,CRI}, \Sigma_{i,sub})^2} \tag{25}$$

are the weighting factors. The total weight w_i is found using

$$\begin{aligned} w_i &= \frac{c_{i,CRI}^{total}}{\sigma(\mathbf{p}_{i,sub}|\mathbf{p}_{i,CRI}, \Sigma_{i,CRI})^2} \\ &+ \frac{c_{i,sub}^{total}}{\sigma(\mathbf{p}_{i,CRI}|\mathbf{p}_{i,CRI}, \Sigma_{i,sub})^2} \end{aligned} \tag{26}$$

where both the denominator terms are unit variance terms. For example, $\sigma(\mathbf{p}_{i,sub}|\mathbf{p}_{i,CRI}, \Sigma_{i,CRI})^2$ represents the variance along the line from $\mathbf{p}_{i,CRI}$ to $\mathbf{p}_{i,sub}$ given that $\Sigma_{i,CRI}$ is the covariance associated with $\mathbf{p}_{i,CRI}$ [9, 10]. The scalar equivalent variance function is explained in Appendix B. Once all scans have been merged into the composite range image, the quality weighted covariance from (22) is retained for each measurement but the total within-scan quality from (23) is discarded as no longer being required.

B. Experimental results

For this experiment, all scans were performed using a prototype medium-range (1 to 10 metre range) laser spot range scanner developed by the National Research Council of Canada. Data processing consisted of applying a 7×7 median filter to the anchor scan and a 25×25 median filter to each subscan to reduce measurement noise. The outlier threshold value was $c_{threshold}^{out} = 0.5$, reflectivity discontinuities were detected using a 3×3 Sobel filter with edge threshold $E_{threshold}^{ref} = 0.1$, the target surface resolution was $\Delta x = 2$ millimetres, the maximum acceptable surface orientation was $\gamma_{max} = \frac{\pi}{4}$, the range limits were $R_{max} = 4$ metres and $R_{min} = 1$ metre, and the reflectivity limits were $\rho_{min} = 0$ and $\rho_{max} = 2$. The anchor and subscans consisted of 256×256 element raster scans and were assumed to have a 14-element acceleration and deceleration region at the start and end of each scan line in which measurement values would be zeroed by the laser range scanner control system. Individual-quality assessment of the anchor scans used $N(\mathbf{p}_i)$ defined as the set of all 8 measurements that surround $\mathbf{p}_i$. Individual-quality assessment of the composite range image was based on $N(\mathbf{p}_i)$ defined as the set of all $\mathbf{p}_j \in N(\mathbf{p}_i)$ that share a single Delaunay edge. Determination of the optimal weighting factor values was not part of the study so the total-quality assessment of the composite range image used $w_{aug} = 0.5$ and $w_{plane} = w_{enc} = w_{blur} = w_{alias} = w_{out} = 0.2$.

The effect of parallax was assumed to be negligible so distance to the beam waist was assumed to be constant; specifically, $R_{spot}(\theta, \phi_i) = 1.40$ metres [9].

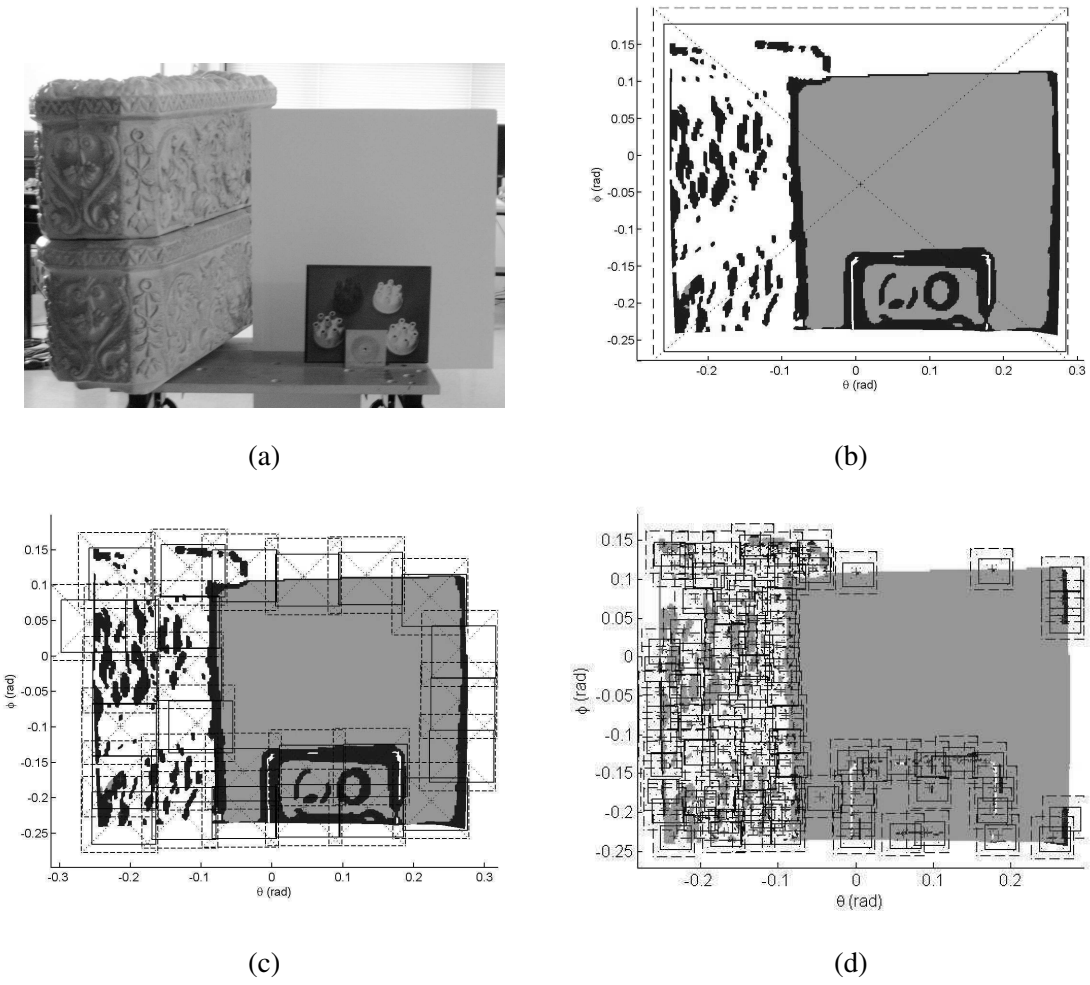

Figure 4: Experiment used to illustrate the adaptive scanning technique. (a) Target object, (b) region map, (c) first set of subscans, and (d) second set of subscans.

Figure 4 illustrates the adaptive scanning processing using one of the test surfaces. Figure 4(a) shows one of the test surfaces used during the course of this investigation. The large planar surface was used for calibration of the laser range scanner's uncertainty and reflectivity models so represents a near-ideal surface for scanning purposes. In front of the posterboard is a picture of four distributor caps which is a planar surface that features reflectivity discontinuities. To the left of the planar surface is a large plastic planter with a spatially-complex surface and an average surface normal that is highly oriented with respect to the line-of-sight of the scanner. The picture of distributor caps is located 1 centimeter in front of the posterboard so represents a source of

range discontinuities, while the top and side of the posterboard represent a truncated surface in which the farther surface is beyond the range of the scanner.

The first step in the adaptive scanning process was to perform a low-density scan of the total field of view. The quality metrics described in Section II were computed for all measurements and the quality assessment described in Section III was used to generate the region map shown in Figure 4(b). The Uscannable region is shown in white, the Complete region in light grey, and the Rescan region in dark grey.

The second step in the process was to generate a series of subscans to completely cover the Rescan region while minimally covering the Unscannable region as described in Section III. Figure 4(c) shows the placement of the first series of subscans. Each dashed box in Figure 4(b) represents the area expected to be covered by a scan while the solid box represents the region within which usable measurements should be obtained.

The third step in the process was to removed from the region map the portions of the Rescan region that had been completely covered by each subscan. the quality metrics described in Section II were then computed for all measurements in each subscan. Areas of each subscan that contained aliased measurements were added to the rescan region to form an updated region map. A second set of subscans was then performed to completely cover the updated Rescan region while minimizing coverage of the Unscannable region after the intersample distance was reduced to compensate for the degree of aliasing detected. Figure 4(d) shows the placement of the second series of subscans. As a result, the subscans in Figure 4(d) are smaller than those in Figure 4(c).

Table I shows the results of 5 experiments using the adaptive scanning method. Scan time efficiency is the total scan+processing time using the adaptive scanning approach divided by the total scan+processing time for a high-density scan of the total field of view. The scan+processing time for a high-density scan is the same for all experiments because the same field of view is used in all cases. Sampling efficiency was similarly calculated by dividing the number of measurements in the composite range image by the number that would be in a high-density scan of the total field of view. The size of the total field of view and sampling density used in a high-density scan is the same in all experiments so the number of measurements collected is the same. In all cases, scan time and sampling efficiencies were less than 25%, where smaller efficiency values are better. For comparison, an efficiency value of 100% would indicate a process no more efficient than a high-density scan of the total field of view. These results show that an adaptive scanning approach can take less time and generate fewer measurements than simply performing a high-density scan of

Table I: Scan Time and Sampling Efficiencies versus total field of view

	Fiberglass Head	Wall Section	Pumpkin Statue	Lawn Ornament	Planter
		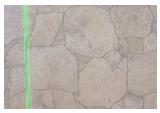			
Total (min)*	58.54	106.35	67.40	108.60	101.80
Scan Time Efficiency†	12.8%	23.3%	14.8%	23.8%	22.3%
Measurements	4,128,768	7,602,176	4,980,736	8,126,464	7,536,640
Sampling Efficiency‡	16.3%	29.9%	19.6%	32.0%	37.4%
	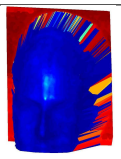	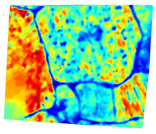	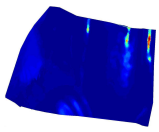	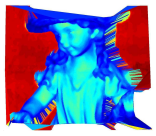	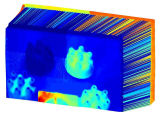

*Total = anchor scan time + total scan time for all subscans + processing time for all scans

†Scan Time Efficiency is versus total field of view scan + processing time = 456.68 minutes, which is the same for all experiments.

‡Sampling Efficiency is versus number of samples from the total field of view scan = 25,396,875 measurements, which is the same for all experiments.

the total field of view, but the degree of improvement depends on the surface complexity so will be highly scene-dependent. The last row in Table I shows a portion of the final model from each experiment after merging all anchor and subscans using the adaptive scanning approach.

IV. DISCUSSION

The experimental results indicate that a considerable reduction in scanning time and number of measurements is possible; however, the cost of these reductions is also a reduction in final model accuracy compared to one generated from performing a high-density scan of the total field of view. For example, if all measurements in a region have a high Planarity quality, this means that the level of non-planarity based on a low-density scan is low, but using a low-density scan means that fine surface details will be missed. This approach, therefore, is only useful if fine model detail is not required, such as when generating a CAD model of a structure. The adaptive scanning approach

represents a trade-off between final model quality and both scanning time and the size of the final model.

The quality metrics presented in this study were the result of a thorough assessment of the various parameters that can affect the quality of a measurement in a range image generated by a laser range scanner. In particular, the resolvability, blur, and sampling quality metrics arose from a study of the effect of spot size, shape and motion on the quality of measurements in a range image. Blur and sampling quality metrics represented a way to weight measurement quality toward measurements obtained from subscans (that have higher blur and sampling quality) over the anchor scan (that have lower blur and sampling quality) without simply discarding the anchor scan data within subscanned regions. Similarly, planarity, outlier, and enclosed quality of measurements from a region can vary depending upon whether they were generated from the anchor scan or one of the subscans because they are neighbourhood-based metrics. Once again, it was important to include them when merging anchor scan and subscan measurements so that their effect would be considered when weighting spatially-close measurements. All quality metrics were used generating the total measurement quality because the total quality of a measurement should represent the contribution of all quality parameters.

In Section I it was proposed that the adaptive scanning approach could be used as part of a view-planning strategy. Specifically, the resolvability, range, and orientation quality metrics can be used to suggest new scanner positions that might result in an improvement in the quality of measurements obtained. Experiments were performed to explore the use of quality metrics in view planning. An anchor scan was obtained from a randomly-selected viewpoint, then a predictive quality assessment was performed in which a virtual version of the scanner was moved in a direction that maximized the resolvability, range, and orientation quality metrics. The scanner was then moved to the position indicated by the predictive quality assessment and the process was repeated. In experiments using all five test surfaces, an optimal location was obtained after no more than three iterations, demonstrating that quality metrics could be used to successfully test alternative viewpoints prior to moving the scanner. An example of the predictive quality assessment approach is shown in Figure 5 [9]. In a view-planning strategy, a predictive quality assessment would be performed only for regions of the model with low orientation, resolvability, or range quality while minimizing coverage of model regions that already have high total quality.

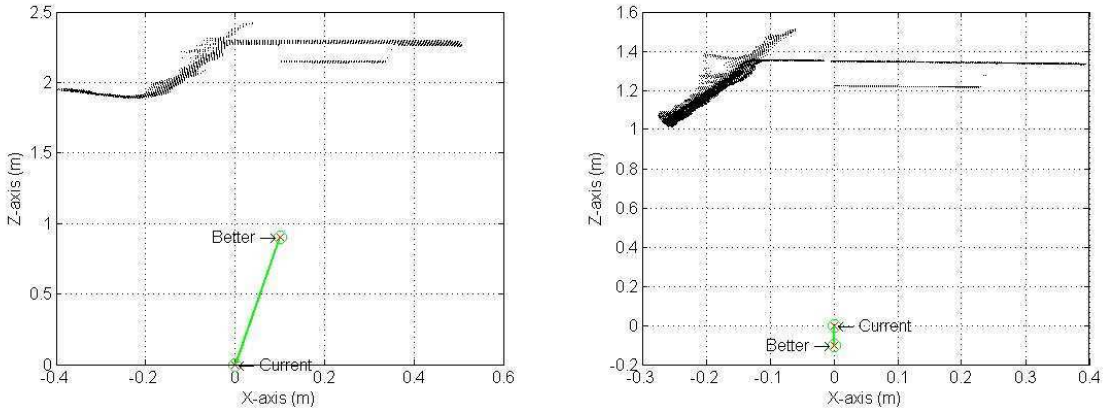

(a) (b)

Figure 5: Experiment to explore view-planning. (a) Initial viewpoint and next best viewpoint based on predictive quality assessment. (b) Second viewpoint and predicted next best viewpoint. A predictive quality assessment of the third viewpoint indicated no other viewpoint will maximize orientation, resolvability, and range quality metrics.

V. CONCLUSIONS

The adaptive scanning method presented in this paper can significantly reduce both the total time spent scanning the surface and the total number of samples acquired to generate a range image from a single viewpoint. Experiments show that this method can take approximately 24% of the time and generate approximately 37% of the measurements compared to a high density scan of the total field of view. Six new quality metrics were developed for the adaptive scanning method: Return, Enclosed, Outlier, Planarity, Resolvability, and Blur. The outlier quality metric was used to identify areas in which measurements were highly variable, such as near spatial and intensity discontinuities. The planarity quality metric was used to identify areas that could be represented as a planar surface so would require few measurements to characterize. The return quality metric was used to identify areas of the initial scan from which it was unlikely that useful measurements could be obtained. Four improved quality metrics were also presented: Orientation, Reflectivity, Range and Sampling. The Sampling quality metric was used to establish an upper-bound on the sample density to ensure that the sampling density was sufficiently high to capture surface details at the target resolution where necessary. The Reflectivity, Resolvability, Orientation, Return, and Range quality metrics were used to define the boundaries of the scannable region for a given viewpoint. All metrics were combined into a Total quality metric which was then used to merge measurements

from all scans that were statistically close based on their quality-weighted covariance into a single composite range image. The resulting composite range image contains fewer measurements than would result from simply combining multiple scans, and the measurement covariances accurately reflect the reduction in measurement uncertainty resulting from the quality-weighted averaging of spatially close measurements.

Appendix A: AXIAL DIMENSIONS IN THE MID-FIELD

The surface dimensions of the region illuminated by the laser beam can be obtained for mid-field measurements if the surface is assumed to be strictly planar within the beam footprint. Consider Figure 2(a) which illustrates the intersection of the laser beam with a surface angled ρ_i with respect to the laser path. The spot radius $w(\zeta)$ a distance ζ from the beam waist can be found by

$$w(\zeta) = w(0)\sqrt{1+\left(\frac{\zeta}{\zeta_0}\right)^2} \tag{A1}$$

where $w(0)$ is the radius of the beam waist and ζ_0 is the depth of focus [13]. Equation (A1) can be rewritten as

$$\zeta_0^2 w(\zeta)^2 = \zeta_0^2 w_0^2 + \zeta^2 w_0^2 \tag{A2}$$

where we have used $w_0 = w(0)$ to simplify the equation.

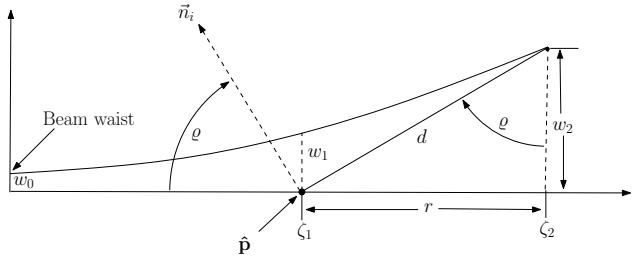

Figure 6: Beam-surface intersection

Figure 6 illustrates the cross-section of the plane intersecting the laser beam. The plane intersects the centre of the beam at a distance ζ_1 from the beam waist, and intersects the $1/e^2$ boundary at ζ_2 from the beam waist. We use $w_1 = w(\zeta_1)$ and $w_2 = w(\zeta_2)$ to represent the widths of the beam at a distance ζ_1 and ζ_2 respectively. The term ζ_1 also represents the distance between the beam waist and the spatial location of the measurement generated by the reflected beam footprint so can be easily obtained. Similarly, w_1 represents the spot radius corresponding to the measurement $\hat{\mathbf{p}}$

so is also easily obtained. Finally, ρ is estimated from the surface normal $\vec{n}_i$ of the neighbourhood regression plane through $\hat{\mathbf{p}}$. What remains is to find d, the surface distance between the peak and edge of the beam footprint.

The terms ζ_2 and w_2 are unknown so need to be eliminated. From Figure 6, we see that

$$\zeta_2 = \zeta_1 + r \tag{A3}$$

where

$$r = d\sin(\rho) \tag{A4}$$

so

$$\zeta_2 = \zeta_1 + d\sin(\rho) \tag{A5}$$

in which all the terms in the right-hand side are known. Similarly

$$w_2 = d\cos(\rho) \tag{A6}$$

is expressed in terms of d and ρ which are also known. Substituting (A5) and (A6) into (A2) results in

$$\zeta_0^2 d^2\cos^2(\rho) = \zeta_0^2 w_0^2 + w_0^2\left(\zeta_1 + d\sin(\rho)\right)^2 \ . \tag{A7}$$

Equation A7 can be expanded in terms of d into an equation of the form

$$d^2K_1 + dK_2 + K_3 = 0 \tag{A8}$$

where

$$K_1 = \left[w_0\sin(\rho)\right]^2 - \left[\zeta_0\cos(\rho)\right]^2 \ , \tag{A9}$$

$$K_2 = 2\zeta_1 w_0^2\sin(\rho) \ , \tag{A10}$$

and

$$K_3 = \left[w_0\zeta_0\right]^2 + \left[w_0\zeta_1\right]^2 \ . \tag{A11}$$

Equation A8 can now be solved using a quadratic equation, generating two possible values of d. These values are the lengths of the long and short axes, representing the cross-section of the intersection of the surface with the $1/e^2$ boundary. Specifically,

$$\{d_{min}, d_{max}\} = \left| \frac{-K_2 \pm \sqrt{(K_2)^2 - 4K_1K_3}}{2K_1} \right| \ . \tag{A12}$$

Equation A2 is symmetrical about the beam waist so this approach holds throughout the mid-field regardless of whether the surface is closer to or farther from the laser with respect to the beam waist. As $\rho \to 0$, $d_{max} \to d_{min}$ and $d_{length} = d_{max} + d_{min} \to d_{width} = 2w_1$ where d_{length} and d_{width} are the length and width of the ovoid beam footprint respectively.

Appendix B: SCALAR-EQUIVALENT VARIANCE

The scalar variance equivalent form is relatively easy to conceptualize when all the elements of the local surface points use the same units of measure; however, in the spherical coordinate system the rotational and radial components have different units of measure. The Mahalanobis distance is a unitless quantity so the elements of the points used to calculate the Mahalanobis distance can be treated as unitless, and the scalar equivalent variance becomes a weighting factor for the unitless Euclidean distance between two points. It can be defined using

$$d^2(\mathbf{p}|\,\mathbf{p}_A, \Sigma_A) = (\mathbf{p}_A - \mathbf{p})^T \Sigma_A^{-1} (\mathbf{p}_A - \mathbf{p}) \tag{B1}$$

where Σ_A is the covariance matrix associated with surface point $\mathbf{p}_A$, and $\sqrt{d^2(\mathbf{p}|\,\mathbf{p}_A, \Sigma_A)}$ is the distance to some point $\mathbf{p}$ in the environment given a measurement $\mathbf{p}_A$ with covariance Σ_A. The $d^2(\mathbf{p}|\,\mathbf{p}_A, \Sigma_A)$ term has a χ^2distribution so $d^2(\mathbf{p}|\,\mathbf{p}_A, \Sigma_A) < \chi^2\left(d_f, \alpha\right)$, where d_f is the number of degrees-of-freedom and α is the probability level, can be used to test whether measurement $\mathbf{p}$ is sufficiently close to the surface point $\mathbf{p}_A$ that it is likely to arise from the surface at probability level α [25, 26].

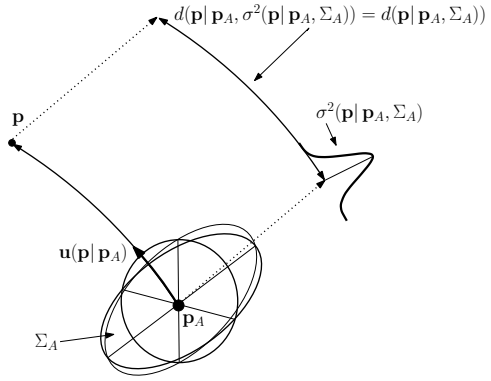

Figure 7: The scalar equivalent variance (SEV) $\sigma^2(\mathbf{p}|\,\mathbf{p}_A, \Sigma_A)$ is the variance along shortest line segment in spherical space to $\mathbf{p}$ given starting point $\mathbf{p}_A$ with covariance Σ_A, and $d(\mathbf{p}|\,\mathbf{p}, \sigma^2(\mathbf{p}|\,\mathbf{p}_A, \Sigma_A))$ is the Mahalanobis distance to $\mathbf{p}$ given starting point $\mathbf{p}_A$ and scalar equivalent variance $\sigma^2(\mathbf{p}|\,\mathbf{p}_A, \Sigma_A)$.

The calculation of the Mahalanobis distance can be simplified by representing the covariance matrix Σ_A as a unitless scalar equivalent variance function $\sigma^2(\mathbf{p}|\,\mathbf{p}_A,\Sigma_A)$ along a unit vector $\mathbf{u}(\mathbf{p}|\,\mathbf{p}_A)$. The scalar equivalent variance is the scalar variance at point $\mathbf{p}$ given a local surface point $\mathbf{p}_A$ with covariance Σ_A, and the unit vector is a vector oriented toward $\mathbf{p}$ given a local surface point $\mathbf{p}_A$. A graphical representation of the scalar equivalent variance can be seen in Figure 7. Consider a line from $\mathbf{p}_A$ to some point in space $\mathbf{p}$ as shown in Figure 7 . If the variance of a cross-section of Σ_A along the shortest path in spherical space from $\mathbf{p}_A$ to $\mathbf{p}$ can be represented by a scalar variance $\sigma^2(\mathbf{p}|\,\mathbf{p}_A,\Sigma_A)$ then (B1) can be rewritten as

$$d^2(\mathbf{p}|\,\mathbf{p}_A,\sigma^2(\mathbf{p}|\,\mathbf{p}_A,\Sigma_A)) = \frac{\|\mathbf{p}_A-\mathbf{p}\|_G^2}{\sigma^2(\mathbf{p}|\,\mathbf{p}_A,\Sigma_A)} \tag{B2}$$

where $\sigma^2(\mathbf{p}|\,\mathbf{p}_A,\Sigma_A)$ is the variance of the Gaussian distribution around $\mathbf{p}_A$ along a line segment in spherical space from $\mathbf{p}_A$ to $\mathbf{p}$. The numerator term $\|\mathbf{p}_A-\mathbf{p}\|_G^2$ is the Euclidean distance between $\mathbf{p}_A$ and $\mathbf{p}$ where $\mathbf{p}_A,\mathbf{p}\in G$ and $G\subset\mathbb{R}^3$ is a bounded region in which:

- the rotational components are bounded such that $\theta\leq\min\{\theta_{max},\pi\}$ and $\theta>\max\{\theta_{min},-\pi\}$ where θ_{max} and θ_{max} are the bounds of the total field of view of the scanner along the θ axis, and $\phi\leq\min\{\phi_{max},\pi\}$ and $\phi>\max\{\phi_{min},-\pi\}$ where ϕ_{max} and ϕ_{max} are the bounds of the total field of view of the scanner along the ϕ axis. This avoids the problem of two radial measure values representing the same spatial point.

- the radial component is restricted to being larger than zero so that no point is allowed to exist at the origin; that is $R>R_{min}>0$.

These restrictions define the boundaries of a region G in the Cartesian space $\mathbb{R}^3$. Points within this space can be represented in either spherical or Cartesian coordinates.

Both (B1) and (B2) express the same distance metric so they can be combined such that

$$\frac{\|\mathbf{p}_A-\mathbf{p}\|_G^2}{\sigma^2(\mathbf{p}|\,\mathbf{p}_A,\Sigma_A)} = (\mathbf{p}_A-\mathbf{p})^T\Sigma_A^{-1}(\mathbf{p}_A-\mathbf{p}) \tag{B3}$$

Rearranging the terms results in

$$\frac{1}{\sigma^2(\mathbf{p}|\,\mathbf{p}_A,\Sigma_A)} = \frac{(\mathbf{p}_A-\mathbf{p})^T}{\|\mathbf{p}_A-\mathbf{p}\|_G}\Sigma_A^{-1}\frac{(\mathbf{p}_A-\mathbf{p})}{\|\mathbf{p}_A-\mathbf{p}\|_G} \tag{B4}$$

in which the first and last terms are unit vectors. These terms can be replaced with a single unit vector $\mathbf{u}(\mathbf{p}|\,\mathbf{p}_A)$. Equation B4 can be rewritten as

$$\sigma^2(\mathbf{p}|\,\mathbf{p}_A,\Sigma_A) = \frac{1}{\mathbf{u}^T(\mathbf{p}|\,\mathbf{p}_A)\Sigma_A^{-1}\mathbf{u}(\mathbf{p}|\,\mathbf{p}_A)} \tag{B5}$$

where

$$\mathbf{u}(\mathbf{p}|\,\mathbf{p}_A) = \frac{\mathbf{p}_A - \mathbf{p}}{\|\mathbf{p}_A - \mathbf{p}\|_G} \tag{B6}$$

Intuitively, (B5) represents the variance in the direction indicated by the unit vector when the unit vector is applied to the covariance matrix. Now, given a known scalar equivalent variance, the Mahalanobis distance can be calculated using (B2).

---

[1] D. MacKinnon, V. Aitken, and F. Blais, "A Review of Measurement Quality Metrics for Range Imaging," *Journal of Electronic Imaging* **17**, September 2008.

[2] V. Sequeira, K. Ng, E. Wolfart, J. G. M. Goncalves, and D. Hogg, "Automated reconstruction of 3D models from real environments," *ISPRS Journal of Photogrammetry and Remote Sensing* **54**, pp. 1–22, February 1999.

[3] M. Callieri, A. Fasano, G. Impoco, P. Cignoni, R. Scopigno, G. Parrini, and G. Biagini, "RoboScan: an automatic system for accurate and unattended 3D scanning," in *Proceedings of the 2nd International Symposium on 3D Data Processing, Visualization and Transmission*, pp. 805–812, 6-9 September 2004.

[4] W. Scott, G. Roth, and J.-F. Rivest, "View Planning for Multi-Stage Object Reconstruction," in *Proceedings of the International Conference on Vision Interface*, pp. 64–71, (Ottawa, ON, Canada), June 2001.

[5] M. Adams, "Lidar design, use, and calibration concepts for correct environmental detection," *IEEE Transactions on Robotics and Automation* **16**, pp. 753–761, December 2000.

[6] J. Hancock, D. Langer, M. Hebert, R. Sullivan, D. Ingimarson, E. Hoffman, M. Mettenleiter, and C. Froehlich, "Active laser radar for high-performance measurements," in *Proceedings of the IEEE International Conference on Robotics and Automation*, **2**, pp. 1465–1470, IEEE, (Leuven, Belgium), 16-20 May 1998.

[7] J.-A. Beraldin, M. Picard, S. El-Hakim, G. Godin, L. Borgeat, F. Blais, E. Paquet, M. Rioux, V. Valzano, and A. Bandiera, "Virtual Reconstruction of Heritage Sites: Opportunities and Challenges Created by 3D Technologies," in *Proceedings of the International Workshop on Recording, Modeling and Visualization of Cultural Heritage*, pp. 141–156, (Ascona, Switzerland), 22-27 May 2005.

[8] A. Johnson, R. Hoffman, J. Osborn, and M. Hebert, "A system for semi-automatic modeling of complex environments," in *Proceedings of the 3rd International Conference on Recent Advances in 3-D*

Digital Imaging and Modeling, pp. 213–220, IEEE, (Ottawa, ON, Canada), 12–15 May 1997.

[9] D. MacKinnon, *Adaptive Laser Range Scanning using Quality Metrics*. Phd dissertation, Carleton University, 2008.

[10] D. MacKinnon, J.-A. Beraldin, L. Cournoyer, and F. Blais, "Evaluating Laser Range Scanner Lateral Resolution in 3D Metrology," in *Proceedings of the IST&T/SPIE 21st Annual Symposium on Electronic Imaging Science and Technology*, (San Jose, CA, USA), 2009.

[11] W. Mendenhall, *Mathematical Statistics with Applictions*, PWS Publishers, Boston, Massachusetts, 3rd ed., 1986.

[12] I. Stamos and P. K. Allen, "3-D Model Construction Using Range and Image Data," in *Proceedings of the IEEE Conference on Computer Vision and Pattern Recognition*, **1**, pp. 531–536, (Hilton Head Island, SC, USA), 13–15 June 2000.

[13] B. Chu, *Laser Light Scattering Basic Principles and Practice*, pp. 156–160. Academic Press, Inc., second ed., 1991.

[14] H. T. Yura, "Atmospheric Turbulence Induced Laser Beam Spread," *Applied Optics* **10**, pp. 2771–2773, December 1971.

[15] R. E. Walker and J. W. McLean, "Lidar Equations for Turbid Media with Pulse Stretching," *Applied Optics* **38**, pp. 2384–2397, April 1999.

[16] R. Baribeau and M. Rioux, "Influence of speckle on laser range finders," *Applied Optics* **30**, pp. 2873–2978, July 1991.

[17] R. Baribeau and M. Rioux, "Centroid fluctuations of speckled targets," *Applied Optics* **30**, pp. 3752–3755, September 1991.

[18] V. Sequeira, K. Ng, E. Wolfart, J. G. Goncalves, and D. Hogg, "Automated 3D reconstruction of interiors with multiple scan-views," in *Proceedings of SPIE*, **3641**, pp. 106–117, 1998.

[19] B. L. Curless, *New methods for surface reconstruction from range images*. PhD Thesis, Stanford University, 1997.

[20] M. Fiocco, G. Boström, J. Gonçalves, and V. Sequeira, "Multisensor fusion for Volumetric Reconstruction of Large Outdoor Areas," in *Proceedings of the Fifth International Conference on 3-D Digital Imaging and Modeling*, pp. 47–54, IEEE, 2005.

[21] M. Soucy, A. Croteau, and D. Laurendeau, "A multi-resolution surface model for compact representation of range images," in *Proceedings of the IEEE International Conference on Robotics and Automation*, **2**, pp. 1701–1706, (Nice, France), 12–14 May 1992.

[22] G. Turk and M. Levoy, "Zippered Polygon Meshes from Range Images," in *Proceedings of SIGGraph*, pp. 311–318, ACM, 1994.

[23] M. Rutishauser, M. Stricker, and M. Trobina, "Merging range images of arbitrarily shaped objects," in *Proceedings of the IEEE Computer Society Conference on Computer Vision and Pattern Recognition*, pp. 573–580, 21–23 June 1994.

[24] A. V. Oppenheim and R. W. Schafer, *Discrete Signal Processing*, Prentice-Hall Signal Processing, Prentice-Hall, Inc., 2 ed., 1999.

[25] J. Neira and J. D. Tardós, "Data Association in Stochastic Mapping Using the Joint Compatibility Test," *IEEE Transactions on Robotics and Automation* **17**, pp. 890–897, December 2001.

[26] I. J. Cox, "A Review of Statistical Data Association Techniques for Motion Correspondence," *International Journal of Computer Vision* **10**(1), pp. 53–66, 1993.

David MacKinnon holds a BSc (90) in Mathematics from the University of Prince Edward Island (PEI), a BSc (01) in Electrical and Computer Engineering from the University of New Brunswick, and both an MASc (03) and PhD (08) in Electrical Engineering from Carleton University, Ottawa. He is currently a Research Associate with the National Research Council Canada's Institute for Information Technology working in the area of measurement standards in 3D metrology. Between 1991 and 1998, he worked as a Statistician, first with the PEI Food Technology Centre, then with the UPEI Clinical Research Centre. He is currently an Engineer-in-Training with the Association of Professional Engineers and Geoscientists of New Brunswick.

Victor Aitken holds a BSc (87) in Electrical Engineering and Mathematics from the University of British Columbia, and the MEng (91) and PhD (95) degrees in Electrical Engineering from Carleton University, Ottawa. He is currently an Associate Professor and Chair of the Department of Systems and Computer Engineering at Carleton University, Ottawa, and is a member of the Professional Engineers of Ontario. His research interests include control systems,

state estimation, data and information fusion, redundancy, sliding mode systems, nonlinear systems, vision, mapping and localization for navigation and guidance of unmanned vehicle systems with applications in underground mining, landmine detection, and exploration.

François Blais is a Principal Research Officer and Group Leader of Visual Information Technology at the National Research Council Canada's Institute for Information Technology. He received his BSc and MSc in Electrical Engineering from Laval University, Quebec City. Since 1984, his research has resulted in the development of a number of innovative 3D sensing technologies licensed to various industries and applications including space and the in-orbit 3D laser inspection of NASA's Space Shuttles. He led numerous R&D initiatives in 3D and the scanning and modeling of important archeological sites and objects of art including the masterpiece Mona Lisa by Leonardo Da Vinci. He received several awards of excellence for his work and is very active on the international scene with scientific committees, more than 150 publications and patents, invited presentations and tutorials.

Table and Figure Captions

Figure 1: Experimental setup

Figure 2: Beam intersection with an angled planar surface results in an oval beam footprint with length d_i^{length} and width $2w(\zeta_i)$ where ζ_i is the distance from the surface to the beam waist along the beam axis. (a) Side view with short axis directed outward from the page (b) top view with normal directed outward from the page.

Figure 3: The range measurement uncertainty of laser range scanners is reduced by integrating $\hat{\mathbf{p}}_i$ with instantaneous beam footprint radius θ_i^{rad} over a distance θ_i^{int}. Integration consists of combining multiple samples into a single measurement.

Figure 4: Experiment used to illustrate the adaptive scanning technique. (a) Target object, (b) region map, (c) first set of subscans, and (d) second set of subscans.

Table 1: Scan Time and Sampling Efficiencies versus total field of view

Figure 5: Experiment to explore view-planning. (a) Initial viewpoint and next best viewpoint based on predictive quality assessment. (b) Second viewpoint and predicted next best viewpoint. A predictive quality assessment of the third viewpoint indicated no other viewpoint will maximize orientation, resolvability, and range quality metrics.

Appendix Figure Captions

Figure 1: Beam-surface intersection

Figure 2: The scalar equivalent variance (SEV) $\sigma^2(\mathbf{p}|\,\mathbf{p}_A, \Sigma_A)$ is the variance along shortest line segment in spherical space to $\mathbf{p}$ given starting point $\mathbf{p}_A$ with covariance Σ_A, and $d(\mathbf{p}|\,\mathbf{p}, \sigma^2(\mathbf{p}|\,\mathbf{p}_A, \Sigma_A))$ is the Mahalanobis distance to $\mathbf{p}$ given starting point $\mathbf{p}_A$ and scalar equivalent variance $\sigma^2(\mathbf{p}|\,\mathbf{p}_A, \Sigma_A)$.